

# Mechanistic Insights into Microsecond Time-Scale Motion of Solid Proteins Using Complementary $^{15}\text{N}$ and $^1\text{H}$ Relaxation Dispersion Techniques

Petra Rovó,<sup>†</sup> Colin A. Smith,<sup>‡,¶</sup> Diego Gauto,<sup>§</sup> Bert L. de Groot,<sup>¶</sup> Paul Schanda,<sup>§</sup> and Rasmus Linser<sup>\*,†,||</sup>

<sup>†</sup>Department Chemie und Pharmazie, Ludwig-Maximilians-Universität München, 81377 München, Germany

<sup>‡</sup>Hall-Atwater Laboratories, Wesleyan University, Middletown, Connecticut 06459, United States

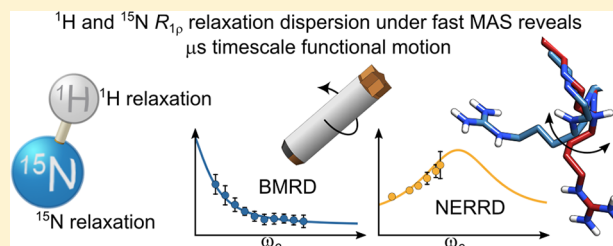
<sup>¶</sup>Department for Theoretical and Computational Biophysics, Max Planck Institute for Biophysical Chemistry, 37077 Göttingen, Germany

<sup>§</sup>Institut de Biologie Structurale (IBS), 38044 Grenoble, France

<sup>||</sup>Faculty of Chemistry and Chemical Biology, Technical University Dortmund, 44227 Dortmund, Germany

## Supporting Information

**ABSTRACT:** NMR relaxation dispersion methods provide a holistic way to observe microsecond time-scale protein backbone motion both in solution and in the solid state. Different nuclei ( $^1\text{H}$  and  $^{15}\text{N}$ ) and different relaxation dispersion techniques (Bloch–McConnell and near-rotary-resonance) give complementary information about the amplitudes and time scales of the conformational dynamics and provide comprehensive insights into the mechanistic details of the structural rearrangements. In this paper, we exemplify the benefits of the combination of various solution- and solid-state relaxation dispersion methods on a microcrystalline protein ( $\alpha$ -spectrin SH3 domain), for which we are able to identify and model the functionally relevant conformational rearrangements around the ligand recognition loop occurring on multiple microsecond time scales. The observed loop motions suggest that the SH3 domain exists in a binding-competent conformation in dynamic equilibrium with a sterically impaired ground-state conformation both in solution and in crystalline form. This inherent plasticity between the interconverting macrostates is compatible with a conformational-preselection model and provides new insights into the recognition mechanisms of SH3 domains.



## INTRODUCTION

There is increasing evidence that many functionally important mechanisms in proteins occur on microsecond-to-millisecond time scales, calling for methods that enable characterization of these motions in a comprehensive and site-specific manner. Magic-angle spinning (MAS) solid-state NMR, in particular, is sensitive to motions over many orders of magnitude, from picoseconds to hours,<sup>1–4</sup> and enables the investigation of insoluble (membrane proteins,<sup>5</sup> amyloids<sup>6</sup>) or large biomacromolecules (virus capsids<sup>7</sup>), as well as crystalline proteins, thus providing fundamental insights into protein motions.

During the past few years, several groups have established that, in the solid state, in addition to the traditional Bloch–McConnell relaxation dispersion (BMRD) approach, which detects conformational dynamics via the fluctuation of the isotropic chemical shift,<sup>8,9</sup> NEar-Rotary-resonance Relaxation Dispersion (NERRD) measurements probe angular amplitudes of microsecond motions.<sup>4,8–23</sup> Thus, these two approaches provide complementary views of  $\mu\text{s}$  dynamics. So far, the most reliable source of microsecond time-scale motion has been the  $^{15}\text{N}$  rotating-frame relaxation.<sup>4,8,9,12–20,22,24,25</sup> The  $^{15}\text{N}$  relaxa-

tion is governed by the heteronuclear  $^1\text{H}$ – $^{15}\text{N}$  dipolar and  $^{15}\text{N}$  chemical shift anisotropy (CSA) interactions, i.e.,  $^{15}\text{N}$  relaxation reports on the  $^1\text{H}$ – $^{15}\text{N}$  bond-vector reorientation. Coherent contributions from unsuppressed anisotropic interactions do not significantly perturb its apparent signal intensity decay provided that high MAS frequencies<sup>26</sup> and deuteration are used.<sup>4</sup> The simplicity of interpretation has made  $^{15}\text{N}$  the prime choice for relaxation dispersion studies.<sup>9,15,19,21</sup> However, the local angular reorientation of individual  $^1\text{H}$ – $^{15}\text{N}$  spin pairs is relatively insensitive to larger-scale collective, translational motions. On the other hand, the slow-time-scale modulation of  $^1\text{H}$ – $^1\text{H}$  dipolar interactions is ideal to grasp these elusive conformational rearrangements.<sup>14,16</sup> Proton NERRD around the HORROR condition, where only homonuclear interactions are sensitively sampled, can sense the apparent change of the proton density in the vicinity of the probe, the motions of back-protonated side chains, and the collective movement of segments with negligible bond-angle

Received: August 28, 2018

Published: January 8, 2019

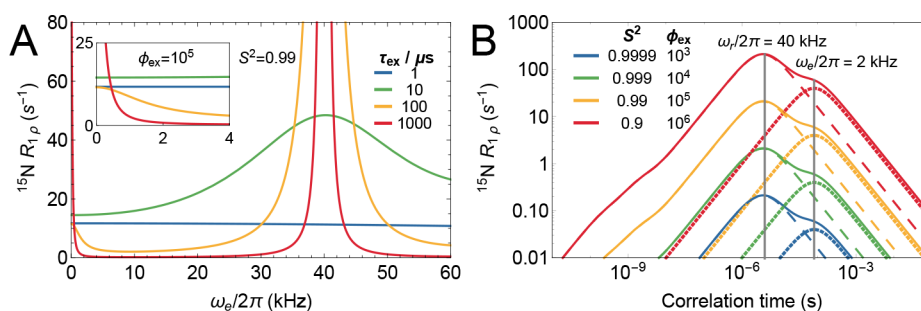


**Figure 1.** Microsecond time-scale motion induces  $^{15}\text{N}$   $R_{1\rho}$  relaxation dispersion in the low-field and high-field regimes. (A) Full, on-resonance  $R_{1\rho}$  relaxation dispersion profile of a hypothetical amide  $^{15}\text{N}$ , which is involved in a motion with an exchange parameter,  $\phi_{\text{ex}} = 10^5 \text{ rad}^2 \text{ s}^{-2}$ , and a slow time-scale order parameter of 0.99. The time scale of motion is varied between  $1 \mu\text{s}$  and  $1 \text{ ms}$ . The inset zooms in on the region corresponding to the Bloch–McConnell RD regime. (B) Correlation-time dependence of  $^{15}\text{N}$   $R_{1\rho}$  relaxation rates assuming increasing microsecond time-scale motional contributions. Dotted, dashed, and solid lines indicate the rates that are the result of the change of only isotropic, only anisotropic, or both isotropic and anisotropic parts of the interaction tensors, respectively. Highest rates are observed when the motion has an exchange frequency ( $k_{\text{ex}} = 1/\tau_{\text{ex}}$ ) matching the probing frequencies (i.e., spinning frequency and/or irradiation frequency). Vertical lines indicate these conditions. The relaxation rates were calculated using eqs 1, 3, and 4, with  $\omega_r/2\pi = 40 \text{ kHz}$ ,  $\omega_e/2\pi = 2 \text{ kHz}$ ,  $\Delta\sigma_{\text{N}} = 170 \text{ ppm}$ , and motional time scales and amplitudes as displayed in the figure.

rotations. In this respect, monitoring both  $^1\text{H}$  and  $^{15}\text{N}$  relaxation rates provides comprehensive insights into the mechanistic details of the protein motion, as they report about complementary aspects of backbone and side-chain fluctuations.

Although the relaxation mechanisms of  $^1\text{H}$  are more complex than those of  $^{15}\text{N}$  (the dense network of  $^1\text{H}$ – $^1\text{H}$  homonuclear dipolar interactions complicates the relaxation mechanisms and also contributes to significant coherent contributions) protons seem to be highly sensitive to motions occurring on the time scale of the spinning frequency; thus, they are well suited for NERRD measurements.<sup>14,16</sup> Therefore, proton relaxation is a particularly sensitive reporter of the microsecond time-scale dynamics, but it conveys only qualitative information on this motion. For quantification, on one hand, the coherent contributions should be fully suppressed; on the other hand, more precise theoretical models are needed which take into account translational motions and multispin interactions. A detailed evaluation on the accuracy of proton relaxation to describe microsecond time-scale motion can be found in the text of [Supporting Information \(SI\)](#) and in ref 16.

To investigate the power of complementary  $^{15}\text{N}$  and  $^1\text{H}$  spin-relaxation measurements in describing  $\mu\text{s}$  dynamics, we used the 62-residue-long chicken  $\alpha$ -spectrin SH3 domain as a model and analyzed its slow conformational dynamics under fast magic-angle-spinning conditions (25–55 kHz spinning frequency). SH3 domains recognize proline-rich ligands with the consensus sequence PxxP.<sup>27,28</sup> They are among the most important elements employed in nature for protein–protein interactions, regulating cell growth, differentiation, apoptosis, transcription, enzymatic regulation, and many more.<sup>29,30</sup> Despite their sequential diversity, their tertiary structure is highly conserved<sup>31</sup> and forms a rigid and structurally stable scaffold for the conformationally more heterogeneous ligand binding surface.<sup>32</sup> Their binding specificity is encoded in the highly variable RT and N-Src loops,<sup>32</sup> the plasticity of which has been associated with ligand recognition and signal transmission toward distal sites by long-range cooperative effects.<sup>31,32</sup> Although SH3 domains have been known for decades, the understanding of the mechanisms behind their specificity and signal transduction through conformational dynamics has remained incomplete. Here we demonstrate that

the combination of different relaxation dispersion methods tailored to assess microsecond time-scale processes is able to identify a previously elusive motional mechanism of an SH3 domain.

The structural and motional properties of this protein in its microcrystalline state have been extensively characterized experimentally, as chicken  $\alpha$ -spectrin SH3 is one of the most studied model systems for solid-state protein NMR pulse-sequence testing.<sup>33–37</sup> It has long been established that this protein preserves both its structure and picosecond–nanosecond time-scale backbone motion in the microcrystalline state as compared to solution state.<sup>6</sup> The  $\beta$ -barrel structure is exceptionally rigid on the picosecond–nanosecond time scale; only the N- and C-terminal residues, as well as the residues at the tip of the loops, show higher motional flexibility.<sup>36,38</sup> Using Bloch–McConnell-type  $^{15}\text{N}$  relaxation dispersion experiments, we have recently demonstrated that the RT and N-Src loops are also involved in slower, microsecond–millisecond time-scale conformational exchange.<sup>21</sup> However, despite the numerous studies on this system over the years, the underlying mechanistic basis has remained elusive.

In this study, the systematic comparison of different  $^{15}\text{N}$  and  $^1\text{H}$  relaxation dispersion profiles helps us to pinpoint the likely mechanism of the microsecond time-scale loop motions. Furthermore, the analysis of hundreds of different SH3 crystal structures provides us with a plausible structural model that can explain these motions. Our findings suggest that the uncovered structural rearrangements are inherent to the SH3 family and potentially serve functional purposes.

## THEORY

In NMR experiments, the time-evolution of a magnetization stems from the stochastic (*incoherent*) and deterministic (*coherent*) modulation of spin Hamiltonians that couple the spin degrees of freedom with the spatial degrees of freedom. For spin 1/2 nuclei, these Hamiltonians include the homo- and heteronuclear dipolar (DD) and scalar couplings and the chemical shift anisotropy (CSA) interactions. For a  $^{15}\text{N}$  spin in the protein backbone, the homonuclear dipolar coupling is negligible, while for a  $^1\text{H}$  in protonated systems it is the dominant interaction. In solid-state NMR dynamics studies, we are interested in the stochastic modulation of the interaction

Hamiltonians that lead to Redfield-type<sup>39</sup> relaxation (anisotropic component) and to exchange broadening (isotropic chemical shift component),<sup>40</sup> and meanwhile we want to suppress the coherent evolution of the magnetization that originates from the very same interaction Hamiltonians. The disentanglement of coherent (static) and incoherent (stochastic) contributions is not trivial, and because the interaction strength scales with the gyromagnetic ratio, the (unwanted) coherent contribution is most problematic for protons.<sup>41,42</sup>

Rotating-frame relaxation in the presence of radiofrequency fields ( $R_{1\rho}$ ) provides a flexible way to probe  $\mu\text{s}$ – $\text{ms}$  dynamics.  $R_{1\rho}$  relaxation dispersion methods follow the change of the relaxation rate constants of the spin-locked magnetization with increasing field strength.<sup>40</sup> Based on the difference between the effective field strength ( $\omega_e$ ) and the spinning frequency ( $\omega_r$ ), two different regimes and thus two different relaxation dispersion methods can be distinguished (Figure 1).

(i) The traditional Bloch–McConnell Relaxation Dispersion (BMRD), which is widely used in solution-state NMR,<sup>40</sup> applies relatively low field strengths with respect to the spinning frequency ( $\omega_e \ll \omega_r$ ) and measures the conformational-exchange-induced contribution to the  $R_{1\rho}$  rates via the modulation of the isotropic chemical shift. Such a dispersion profile can be best approximated with the Bloch–McConnell equation system.<sup>40</sup> In the case of two-site exchange with skewed populations, the solution for rotating-frame relaxation can be expressed as

$$R_{1\rho} = R_1 \cos^2 \theta + R_{1\rho}^0 \sin^2 \theta + \frac{\sin^2 \theta p_1 p_2 \Delta \omega_{12}^2 k_{\text{ex}}}{k_{\text{ex}}^2 + \omega_e^2} \quad (1)$$

where the fitted parameters include the populations ( $p_1, p_2 = 1 - p_1$ ), time scale ( $\tau_{\text{ex}} = 1/k_{\text{ex}}$ ), and baseline relaxation rates of the exchanging sites ( $R_1, R_{1\rho}^0$ ). For fast exchange,  $p_1, p_2$ , and  $\Delta \omega_{12}$  are entangled and only the product of  $\phi_{\text{ex}} = p_1 p_2 \Delta \omega_{12}^2$  can be determined, particularly if measurements are performed at a single magnetic field strength.

(ii) In solid-state magic-angle-spinning measurements, another informative dispersion regime occurs close to the rotary-resonance conditions, where  $\omega_e \approx n \times \omega_r$  and  $n = 0.5, 1, 2$ . Such a dispersion profile is called Near Rotary-Resonance Relaxation Dispersion (NERRD).<sup>14,15</sup> Unlike the case of BMRD, which is due to the differences in isotropic chemical shifts, the NERRD profile is due to fluctuations of the anisotropic Hamiltonian (DD, CSA) and can be considered as a Redfield-type relaxation. Thus, the NERRD profiles can be modeled with analytical relaxation-rate equations that take into account the signal modulation due to magic-angle spinning and rf irradiation.<sup>16,43</sup>

In a recent publication, we discussed the range of validity and accuracy of Redfield relaxation rate equations to describe slow conformational exchange processes in the solid state under magic-angle spinning.<sup>16</sup> Here we only provide the list of equations for homo- and heteronuclear dipolar relaxation ( $R_{1\rho}^{\text{II}}$  and  $R_{1\rho}^{\text{IS}}$ ) and chemical shift anisotropy relaxation ( $R_{1\rho}^{\text{CSA}}$ ) that are relevant for the current study, and the reader is referred to refs 16 and 4 for detailed theoretical aspects.

$$R_{1\rho}^{\text{II}} = \frac{3}{16} d_{\text{II}}^2 \{ J(2\omega_e - 2\omega_r) + 2J(2\omega_e - \omega_r) + 2J(2\omega_e + \omega_r) + J(2\omega_e + 2\omega_r) + 10J(\omega_1) + 4J(2\omega_1) \} \quad (2)$$

$$R_{1\rho}^{\text{IS}} = \frac{1}{8} d_{\text{IS}}^2 \left\{ \frac{2}{3} J(\omega_e - 2\omega_r) + \frac{4}{3} J(\omega_e - \omega_r) + \frac{4}{3} J(\omega_e + \omega_r) + \frac{2}{3} J(\omega_e + 2\omega_r) + J(\omega_1 - \omega_s) + 3J(\omega_s) + 6J(\omega_1) + 6J(\omega_1 + \omega_s) \right\} \quad (3)$$

$$R_{1\rho}^{\text{CSA}} = \frac{\omega_s^2 \Delta \sigma^2}{18} \left\{ \frac{2}{3} J(\omega_e - 2\omega_r) + \frac{4}{3} J(\omega_e - \omega_r) + \frac{4}{3} J(\omega_e + \omega_r) + \frac{2}{3} J(\omega_e + 2\omega_r) + 3J(\omega_s) \right\} \quad (4)$$

In the above equations,  $d_{\text{II}} = -\frac{\mu_0 \gamma_{\text{I}} \gamma_{\text{S}} \hbar}{4\pi \langle r_{\text{II}}^3 \rangle}$  and  $d_{\text{IS}} = -\frac{\mu_0 \gamma_{\text{I}} \gamma_{\text{S}} \hbar}{4\pi \langle r_{\text{IS}}^3 \rangle}$  are the homo- and heteronuclear dipolar coupling constants, respectively,  $\Delta \sigma$  is the reduced chemical shift anisotropy, and  $\omega_1$  and  $\omega_s$  are the Larmor frequencies of  $^1\text{H}$  and  $^{15}\text{N}$ , respectively.

The simplest form for the spectral density function in the solid state can be defined as

$$J(\omega) = \frac{2}{5} \left( (1 - S^2) \frac{\tau_c}{1 + (\omega \tau_c)^2} \right) \quad (5)$$

where  $\tau_c$  is the correlation time of the motion and  $S^2$  is the generalized order parameter. To cover a wider time-scale range, more complex spectral density functions can be introduced; however, the validity of such models to accurately present motions in the solid state has been recently questioned.<sup>17,20</sup> Elevated relaxation rate constants close to the rotary-resonance conditions are the consequence of microsecond time-scale motion<sup>9</sup> as demonstrated in Figure 1. Accordingly, by following the change of the  $R_{1\rho}$  rates as a function of the applied rf field strength (and/or spinning frequency), one can gain insight into the protein internal dynamics that occurs on this time-scale regime.<sup>4,9,14,15,18</sup> In on-resonance  $R_{1\rho}$  experiments, the homonuclear dipolar  $R_{1\rho}$  depends on spectral densities evaluated at  $2\omega_e \pm \omega_r$  and  $2\omega_e \pm 2\omega_r$ , which are at the half- and full-rotary resonance conditions (the half-rotary resonance condition is best known as HORROR condition), while the heteronuclear dipolar and CSA relaxation depend on spectral densities at  $\omega_e \pm \omega_r$  and  $\omega_e \pm 2\omega_r$ , which correspond to the  $n = 1$  and  $n = 2$  rotary-resonance conditions. As a consequence, in case of a microsecond time-scale fluctuation, the NERRD “bumps” appear at (a factor of 2) lower rf fields for homonuclear dipolar than for heteronuclear dipolar and CSA relaxation.

## ■ MATERIALS AND METHODS

**Sample Preparation.** For solid-state NMR measurements, perdeuterated, uniformly  $^{15}\text{N}$  or  $^{15}\text{N}/^{13}\text{C}$ -labeled SH3 samples were prepared using the protocols described in the literature.<sup>33</sup> To accelerate data acquisition, the samples were doped with 75 mM Cu-EDTA.<sup>34</sup> Cu-doping accelerates the  $^1\text{H}$  longitudinal relaxation and slightly elevates the baseline  $R_{1\rho}$  rates of both  $^1\text{H}$  and  $^{15}\text{N}$ ,<sup>34,44</sup> but it has no effect on the relaxation dispersion. The lyophilized samples were redissolved either in a 30:70 ratio mixture of  $\text{H}_2\text{O}/\text{D}_2\text{O}$  or in pure  $\text{H}_2\text{O}$  (pH = 7), such that the samples were partially or fully protonated at labile sites. The samples were filled into 2.5 mm and 1.3 mm rotors. For chemical-shift referencing and for temperature calibrations, the DSS methyl signal was used as internal standard.



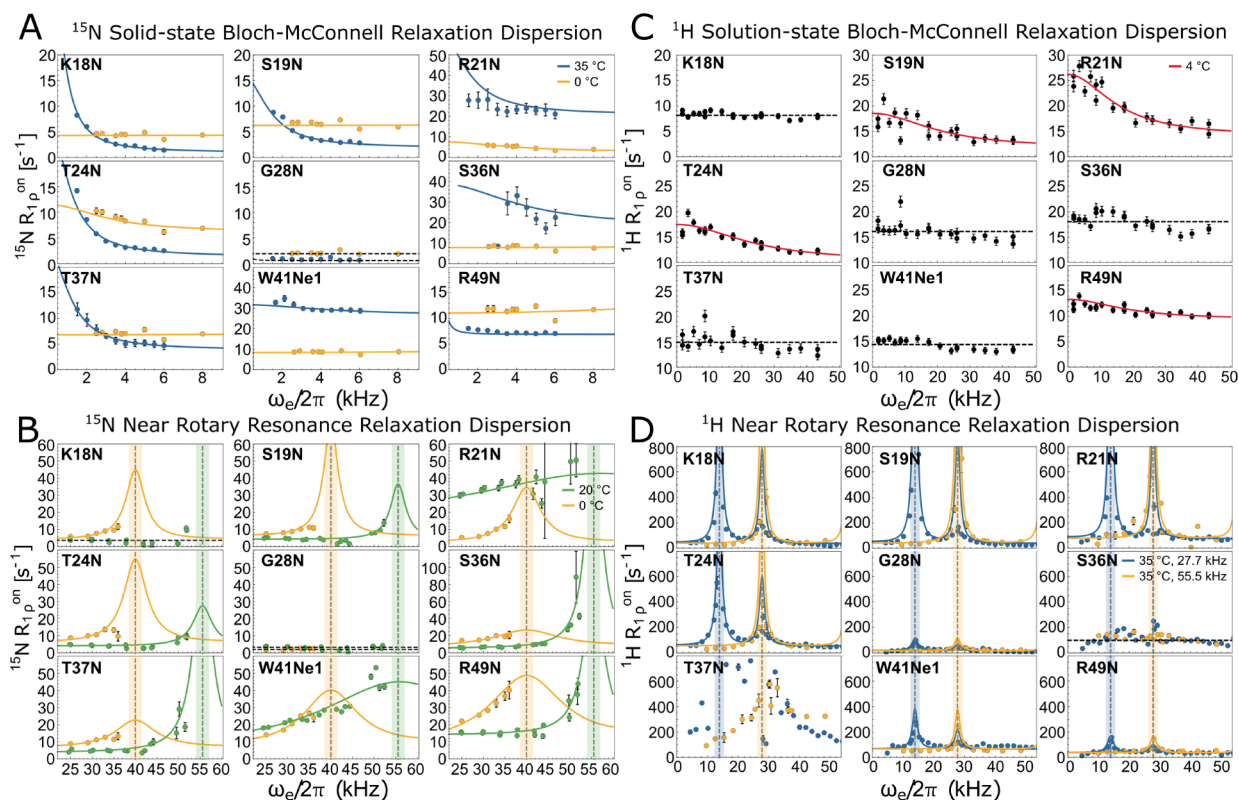


**Figure 2.**  $^{15}\text{N}$  and  $^1\text{H}$  relaxation dispersion profiles of selected residues of SH3 measured in solid and solution states. (A)  $^{15}\text{N}$  BMRD profiles obtained at 35 °C (blue) at 27.77 kHz spinning frequency at 600 MHz on a 30% back-exchanged sample, and at 0 °C (yellow) at 40.00 kHz spinning frequency at 600 MHz on a 30% back-exchanged sample. (B)  $^{15}\text{N}$  NERRD profiles obtained at 0 °C (yellow) at 40.00 kHz spinning frequency at 600 MHz on a 30% back-exchanged sample, and at 20 °C (green) at 55.55 kHz spinning frequency at 700 MHz on a 100% back-exchanged sample. (C) Solution-state, off-resonance  $^1\text{H}$  BMRD profiles obtained at  $\sim 4$  °C at 600 MHz. (D)  $^1\text{H}$  on-resonance NERRD profiles obtained at  $\sim 35$  °C using 27.77 kHz MAS at 600 MHz (blue) and at 55.55 kHz MAS at 800 MHz (yellow). Both samples were 30% proton back-exchanged. The off-resonance  $R_{1\rho}$  rate constants are back-calculated to 90°. The rotary-resonance and HORROR conditions are indicated with vertical dashed lines;  $\pm 1.5$  kHz wide boxes mark the region that should be avoided during NERRD measurements. In both A and B, solid lines show the results of the relaxation-dispersion profile fits, the yellow line in A and B are the result of the joint fit using the same exchange time-scale parameters (see text in SI for details of the fits). The full list of  $^{15}\text{N}$  dispersion profiles can be found in Figure S6. In C, solid lines show the results of the Bloch–McConnell relaxation-dispersion profile fits. In D, solid blue and yellow lines show the tentative fits of eq 2 to the on-resonance  $^1\text{H}$  NERRD data. The full list of  $^1\text{H}$  dispersion profiles can be found in Figure S7. In A–D, dashed lines indicate the baseline relaxation rates wherever no significant microsecond–millisecond time-scale motion could be detected.

For solution-state studies,  $^2\text{H}$ ,  $^{13}\text{C}$ -,  $^{15}\text{N}$ -labeled SH3 sample was dissolved in a 20 mM citrate buffer (pH = 3) containing 30%  $\text{H}_2\text{O}$  and 70%  $\text{D}_2\text{O}$ , and 280  $\mu\text{L}$  was loaded into a 5 mm Shigemitsu tube. The final protein concentration was 0.5 mM.

**Solid-State NMR Measurements.** Magic-angle-spinning solid-state NMR spectra were recorded on Bruker 600 MHz (14.1 T), 700 MHz (16.4 T), and 800 MHz (18.8 T) spectrometers. Samples were spun at 27.7, 40.0, and 55.5 kHz.  $^1\text{H}$  chemical shifts were internally referenced to the methyl signal of DSS (0 ppm). Sample temperature was assessed by the shift difference between the signals of DSS methyl and water protons, and rf-induced heating was monitored and corrected for by the HN chemical shift of A56 of SH3, which seems to be a highly temperature-sensitive residue.

**Solution-State NMR Measurements.** Solution-state NMR experiments were carried out on a Bruker Avance spectrometer operating at 600 MHz  $^1\text{H}$  Larmor frequency, and the effective sample temperature was adjusted to  $\sim 4$  °C. The measurement and analysis procedure followed previously published protocols.<sup>45,46</sup>

The details of the various samples used in each experiment, the measurement conditions, the acquisition parameters, the pulse sequence schemes, the data analysis, and the description of the structural bioinformatics analysis can be found in the text of SI.<sup>47–55</sup>

## RESULTS AND DISCUSSION

**$^{15}\text{N}$  Relaxation.** A recent analysis of the  $^{15}\text{N}$  BMRD profiles of the SH3 domain<sup>21</sup> showed that significant hundreds-of-microsecond-time-scale motion occurs in certain regions of the protein at 35 °C (see Table S1 for the obtained motional parameters). These motions are localized around the RT (Q16–T24) and N-Src loops (N35–N38). Particularly high exchange amplitudes ( $\phi_{\text{ex}}$ ) were detected for R21, T24, T37, N38 backbone and N35 side-chain nitrogens. The observed substantial relaxation dispersion highlights that the chemical environment of many residues is generally altered upon the conformational-exchange process. To elucidate the mechanism that led to these large effects, we analyzed a comprehensive series of relaxation dispersion profiles, including solid-state  $^{15}\text{N}$  BMRD and NERRD (Figure 2A,B), solution-state  $^1\text{H}$  BMRD, and solid-state  $^1\text{H}$  NERRD experiments (Figure 2C,D) measured on perdeuterated, 30%, or 100% labile-proton back-exchanged samples (see methods in SI for the detailed list of measurement conditions).

Our first  $^{15}\text{N}$  data set was recorded on a 30% back-exchanged sample with 40 kHz spinning frequency using on-resonance spin-locks, and the temperature was set to as low as

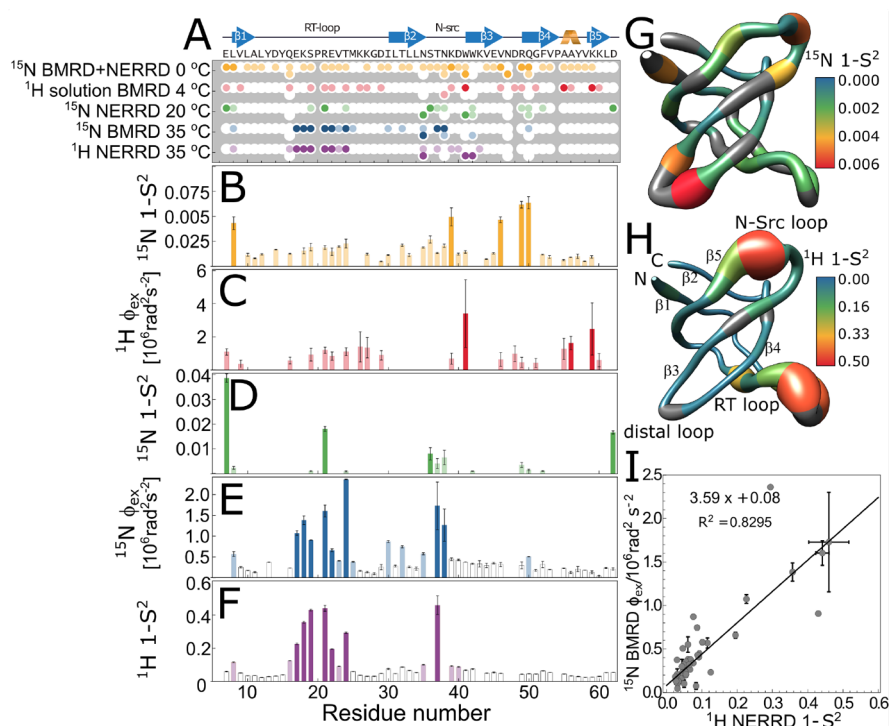


**Figure 3.** Motional amplitudes derived from the different relaxation dispersion experiments. (A) Microsecond time-scale motion is detected for various backbone and side-chain sites in SH3. From top to bottom: solid-state  $^{15}\text{N}$  BMRD and NERRD measured at  $\omega_r/2\pi = 40$  kHz spinning frequency at  $0^\circ\text{C}$  (yellow); solution-state  $^1\text{H}$  BMRD measured at  $4^\circ\text{C}$  (red); solid-state  $^{15}\text{N}$  NERRD measured at  $\omega_r/2\pi = 55.55$  kHz spinning frequency at  $20^\circ\text{C}$  (green); solid-state  $^{15}\text{N}$  BMRD measured at  $\omega_r/2\pi = 27.77$  kHz spinning frequency at  $35^\circ\text{C}$  (blue); solid-state  $^1\text{H}$  NERRD measured at  $\omega_r/2\pi = 27.77$  and  $55.55$  kHz spinning frequencies at  $35^\circ\text{C}$  (purple). In A, B, C, D, and F, darker shades denote the sites with higher than average motional amplitudes; the corresponding amplitudes ( $1 - S^2$  and  $\phi_{\text{ex}}$ ) are plotted in B, C, D, E, and F, using the same color code. In E and F, open bars indicate the sites for which the fitting model, that includes microsecond time-scale exchange contribution, was significantly better than the no-exchange model ( $p < 0.005$ ); however, the obtained motional amplitudes ( $1 - S^2$  and  $\phi_{\text{ex}}$ ) are relatively low. The values in E were derived from the G and H “sausage” representation of the local fast (G) and slow (H) microsecond dynamics derived from the amplitudes displayed in B and F, respectively. (I) Linear correlation between the  $^1\text{H}$  (apparent) order parameter (expressed as  $1 - S^2$ ) and  $^{15}\text{N}$  BMRD exchange amplitudes ( $\phi_{\text{ex}}$ ). Only the backbone amide protons and nitrogens were included in the linear regression.

possible ( $\sim 0^\circ\text{C}$ ) to avoid detrimental rf heating at high rf fields. Here the  $^{15}\text{N}$  relaxation dispersion series spans both the low (BMRD) and the high (NERRD) rf field regimes (yellow dots in Figure 2A,B). Another series was measured at higher spinning frequencies (55.55 kHz) on a 100% back-exchanged sample, where we used off-resonance spin-locks at  $\pm 35.3^\circ$  tilt angle (green dots in Figure 2B). At this condition  $\omega_e = \sqrt{3}\omega_1$ , i.e., the applied rf field is  $1.73\times$  weaker than what the spins perceive; thus, the rf-induced heating is less problematic. The observed effective sample temperature at this condition was  $\sim 20^\circ\text{C}$ .

Figure 2A,B compares the  $^{15}\text{N}$  BMRD and NERRD profiles of selected residues of SH3 which do (K18, S19, R21, T24, S36, T37, W41N $\epsilon$ 1, R49) or do not (G28) show indications of microsecond time-scale motion at 40 kHz spinning frequency at  $0^\circ\text{C}$ , at 55.55 kHz at  $20^\circ\text{C}$ , and at 27.77 kHz at  $35^\circ\text{C}$ . When analyzed independently, the BMRD profiles at low temperatures (Figure 2A, yellow data points) suggest negligible slow-motional contributions for most  $^{15}\text{N}$  sites, and only R21, V23, and T24 display noticeable dispersion in this region (see Tables S2 and S3 and Figure S6 for the entire list of  $^{15}\text{N}$  BMRD and NERRD profiles and for fitted parameters). However, when the whole profile is measured including the near-rotary-resonance region (Figure 2B, yellow data points), it becomes apparent that all of these sites displayed in Figure 2A (except G28 as an example of a rigid residue) are involved in

low-amplitude ( $S^2 \approx 0.998$ ) fast microsecond time-scale motion ( $\tau_{\text{ex}} \approx 20\text{--}50 \mu\text{s}$ ). For the low-temperature data set, the  $^{15}\text{N}$  BMRD and NERRD profiles were fitted simultaneously with one common motional time scale ( $\tau_{\text{ex}}$ ); the other fitted parameters include the baseline  $R_{1\rho}$  rate constant, which incorporates all the fast picosecond–nanosecond time-scale motional contributions,  $\phi_{\text{ex}}$ , which corresponds to the amplitude of the BMRD profile, and the order parameter  $S^2$ , which represents the amplitude of the angular motion. The highest NERRD effect is detected for two distal loop residues (R49 and Q50), with an order parameter of 0.994 and time scale of  $\sim 15\text{--}35 \mu\text{s}$ , and to a lesser extent for E7, K39, and V46 (see Figure 3B for an overview of the obtained order parameters). The absence of observable BMRD for the sites with high NERRD can be explained by the low population of the excited state and/or a negligible  $^{15}\text{N}$  chemical shift difference between ground and excited states, as well as by the fact that  $\sim 30 \mu\text{s}$  time-scale exchange processes result in relatively shallow dispersion (cf. inset in Figure 1A). This observation highlights the complementary nature of  $^{15}\text{N}$  BMRD and NERRD measurements and implies that the two methods do not necessarily validate each other.

In comparison to the low-temperature profiles (Figure 2A yellow data points), some sites, namely R21, S36, N38, and W41N $\epsilon$ 1, display significantly elevated baseline  $^{15}\text{N}$   $R_{1\rho}$  rates at higher ( $35^\circ\text{C}$ ) temperatures (Figure 2A blue data points),

which can be explained by an increase of the amplitude of their fast, hundreds of ns to few  $\mu$ s, time-scale motion. This observation is confirmed by the NERRD measurements at 20 °C (Figure 2B and Figure 3D, green data points), where the NERRD profiles of R21 and W41N $\epsilon$ 1 indicate a motion that occurs on the 4–7  $\mu$ s time scale, with an order parameter of 0.98, and the profiles of S36 and N38 report on a somewhat faster (50–80  $\mu$ s) and more restricted motion ( $S^2 = 0.992$ –0.995). The NERRD profiles of most other sites are flattened out, which suggests that their fast microsecond time-scale motion has accelerated from the 20–50  $\mu$ s at 0 °C to the 0.1–5  $\mu$ s regime at 35 °C, thereby escaping the detection regime of both BMRD and NERRD experiments. (This is also confirmed by the overall decrease of the  $^{15}\text{N}$   $R_{1\rho}$  baseline relaxation rates.)

Interestingly, the high-temperature  $^{15}\text{N}$  BMRD profiles of these residues report on a different aspect of the conformational rearrangements (Figure 2A, blue data points). Here increasing the temperature apparently changes the observed time scale of motion from the 20–50  $\mu$ s to hundreds of  $\mu$ s regime (Figure 2A, blue data points). While this is seemingly in conflict with an expected increase in the rate of motion, it can be explained by considering that more than just one characteristic time scale of motion is present,<sup>17</sup> i.e., a faster one at  $\sim$ 1–50  $\mu$ s, and a slower one at  $\sim$ 300–500  $\mu$ s time scales. Multiple time-scale models, such as the one in the extended model-free approach,<sup>56</sup> are regularly used to describe fast picosecond–nanosecond motions both in solution state and in solid state.<sup>25,38,57</sup>

The exceptional sensitivity of MAS solid-state  $R_{1\rho}$  measurements to the microsecond time-scale motion enables the reliable differentiation between motions occurring on the tens of  $\mu$ s and hundreds of  $\mu$ s time scales in case a large range of  $\omega_1$  or  $\omega_r$  is sampled (cf. Figure 1A).  $^{15}\text{N}$  NERRD profiles can sensitively detect faster motions (few tens of  $\mu$ s), and  $^{15}\text{N}$  BMRD methods are more sensitive to slower motions (few hundreds of  $\mu$ s). Note that fast microsecond motions produce shallow and extended dispersions at the BMRD regime, which get masked by the rise of the relaxation rate at relatively high rf field strength, where the BMRD and NERRD regimes overlap. On the contrary, the quantification of slow microsecond motions in NERRD profiles would require to approach the resonance conditions much closer (cf. Figure 1A red curve) than it is required for fast microsecond motions. Close to the resonance conditions both relaxation and dipolar and CSA recoupling occur, in which two phenomena cannot be distinguished. Therefore, the combination of  $^{15}\text{N}$  BMRD and NERRD methods is vital to observe motion on multiple time scales.

To gain further insights into the mechanisms behind the microsecond time-scale motions, and to validate the findings of the solid-state  $^{15}\text{N}$  relaxation dispersion experiments, we measured solution-state  $^1\text{H}$  off-resonance BMRD, reporting on changes in isotropic shielding by the environment, and solid-state  $^1\text{H}$  on-resonance NERRD profiles at 27.77 and at 55.55 kHz spinning frequencies (Figure 2C,D), reporting on regional changes in the proton dipolar-coupling network. The low-temperature (4 °C) solution-state BMRD profiles confirm the presence of fast, 10–20  $\mu$ s time-scale motion for various sites (Figure 4). These sites include amide protons in the RT-loop (S19, R21, E22, T24), in the  $\beta$ 2-strand (K26, K27, D29), in the distal-loop (D48, R49), and in the  $3_{10}$  helix (A55, A56) (Figure 3C). The full list of dispersion curves, together with the obtained motional parameters, can be found in Table S4

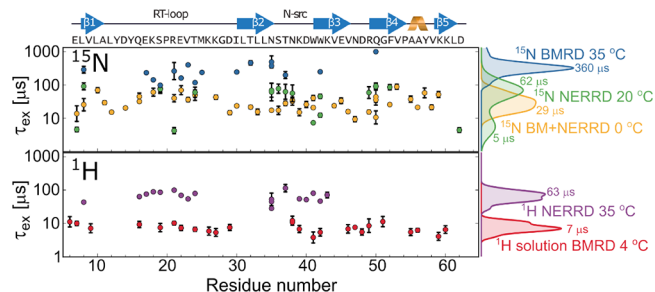


**Figure 4.** Comparison of the obtained exchange-time-scale regimes of the different relaxation dispersion methods. The same color scheme is used as in Figure 3. Exchange time scales are plotted as a function of the residue number for the backbone and side-chain nuclei for which significant microsecond motion was detected. The smoothed time-scale histograms are displayed at the left-hand side of the graph.

and Figure S7. Perdeuteration, and the application of off-resonance spin-locks, with the carrier set both to positive and negative offsets from the center of the spectrum at  $\theta = \pm \arctan(1/\sqrt{2})$  angles, ensure that the measured relaxation rates in solution indeed reflect the microsecond time-scale exchange processes and that cross-relaxation and Hartman–Hahn transfer do not contribute to the magnetization decay.<sup>45</sup>

Our solid-state  $^1\text{H}$  NERRD relaxation measurements, on the other hand, suffer both from cross-relaxation and from coherent contributions; therefore, the parameters obtained from the  $^1\text{H}$  NERRD analysis convey only qualitative information about the motion. Although fast spinning and perdeuteration reduce the detrimental effects of the strong  $^1\text{H}$ – $^1\text{H}$  interaction network on the evolution of proton magnetization, homonuclear dipolar coupling is reintroduced when the spin-lock field strength approaches the half-rotary-resonance (HORROR) condition. As a consequence, in NERRD experiments near the resonance conditions, the proton magnetization evolves both due to increased relaxation and due to dipolar recoupling. Using off-resonance  $R_{1\rho}$  at 35.3° or 54.7° effective tilt angle could help to further reduce the cross-relaxation and the coherent effects; however, even at those conditions the quantification of the  $^1\text{H}$  NERRD data is questionable. If a  $^1\text{H}$  NERRD profile was only a consequence of  $^1\text{H}$ – $^1\text{H}$  homonuclear dipolar relaxation, then, in on-resonance experiments, the NERRD effect would be twice as large at the HORROR condition than at the full-rotary-resonance condition. In our  $^1\text{H}$  NERRD data set, the drastically higher than 2:1 ratio for the  $R_{1\rho}$  rates around the  $n = 0.5$  and  $n = 1$  resonance conditions implies a significant influence of coherent dephasing (recoupling) on the  $^1\text{H}$  relaxation rates around the HORROR condition. It is important to note that the coherent dephasing is much stronger at the HORROR than at the full rotary-resonance condition. This may seem contradictory because at the  $n = 0.5$  condition only the homonuclear dipolar coupling is effective, while at the  $n = 1$  resonance condition, the  $^1\text{H}$ – $^{15}\text{N}$  dipolar and the CSA couplings are reintroduced in addition. However, compared to the homonuclear recoupling at the  $n = 1$  condition, the  $\gamma$ -encoded nature of the homonuclear recoupling at the  $n = 0.5$  condition makes recoupling at the HORROR condition highly efficient.<sup>58</sup> As such, the associated coherent dephasing is much smaller for  $n = 1$  than at the  $n = 0.5$  condition. Besides, coherent contributions in the  $^1\text{H}$  NERRD experiments are also apparent from the high  $^1\text{H}$   $R_{1\rho}$  baseline rates and from the non-negligible NERRD recoupling



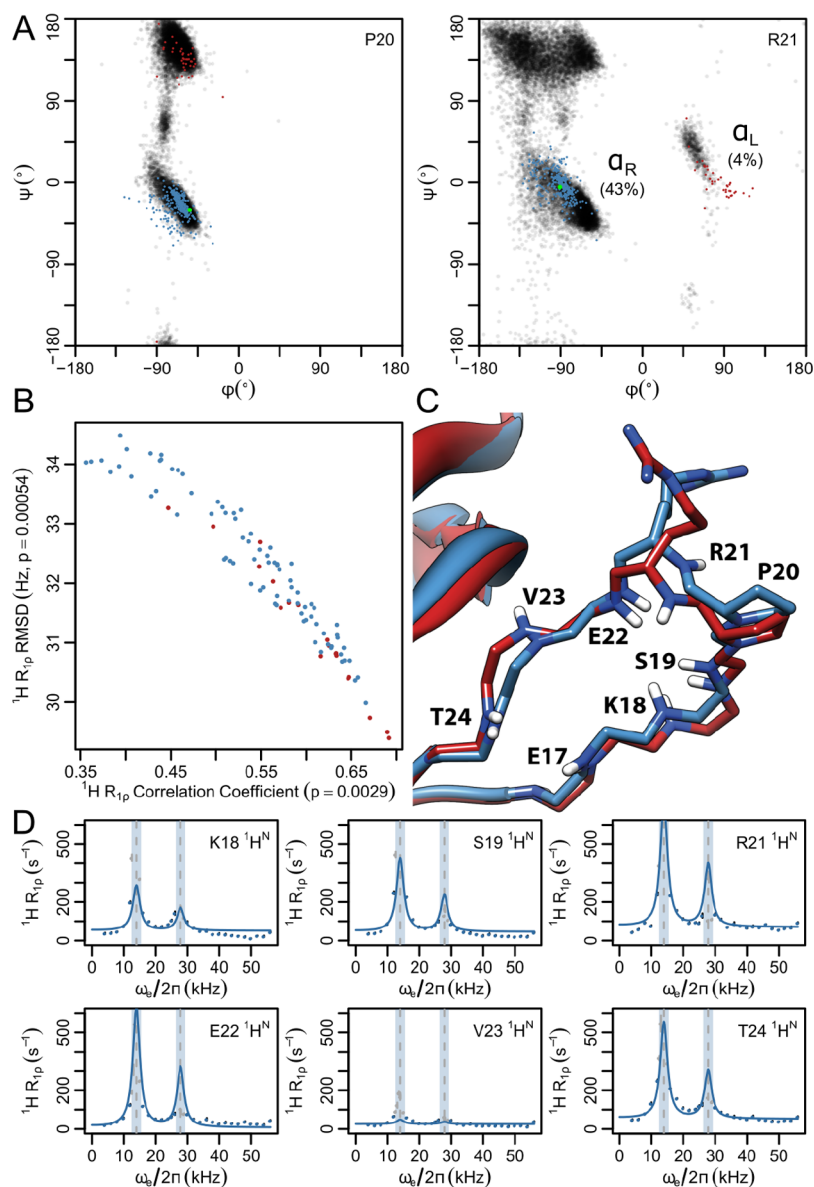


**Figure 5.** A peptide plane flip explains the experimental data. (A) Ramachandran plots of residues aligning with P20 and R21. Blue and red points show the  $\phi/\psi$  angles of the structures with right-handed ( $\alpha_R$ ) or left-handed ( $\alpha_L$ )  $\alpha$ -helix conformations, respectively. The 2NUZ crystal structure is green. Black points show the background distribution found in random-coil regions. (B) By two different scoring metrics,  $\alpha_L$  excited-state conformations (red) show significantly better prediction of the  $^1\text{H } R_{1\rho}$  data than  $\alpha_R$  conformations (blue). A Wilcoxon rank sum test was used to compute the  $p$ -values for the enrichment of  $\alpha_L$  excited states. (C) RT loop structures of the best structural ensemble including the ground-state (2NUZ, blue) and hypothetical excited state (homology modeled from 1SEM: A, red). (D)  $^1\text{H } R_{1\rho}$  curves predicted from the structural ensemble (solid line) compared with experimental data acquired at 600 MHz (dots). Excluded data ranges around the half and full rotary-resonance conditions are shaded.

detected for most rigid sites. SI gives an assessment of errors introduced via coherent effects and stochastic reprotonation in perdeuterated and partially labile-proton-back-exchanged samples.

Despite the inaccuracies in quantification of proton relaxation data, we noticed that in practice, the superposition of relaxation and recoupling in on-resonance  $^1\text{H}$  NERRD experiments identifies the same sites which were described as “dynamic on the microsecond time scale” in the high-temperature  $^{15}\text{N}$  BMRD experiments,<sup>21</sup> a view that has also been supported by  $^1\text{H}$  NERRD data on ubiquitin.<sup>14</sup> In both approaches, the largest apparent dispersions were measured for the residues in the RT-loop (Q16, E17, K18, S19, R21, E22, and T24) and to some extent in the N-Src loop (Figure

3E,F,H). As such, as a qualitative measure, on-resonance  $^1\text{H}$  NERRD measurements sensitively identify the sites which take part in slow (few hundreds  $\mu\text{s}$ ) microsecond time-scale motion; however, the faster processes remain obscure in these measurements.

While the  $^1\text{H}$  NERRD profiles are not solely caused by relaxation, we tentatively fitted them with the homonuclear dipolar relaxation-rate equation (see text in SI for details of the fitting process). With the fitted apparent motional parameters, we get a *relative* measure of the extent of the motion (the fit results for time scales are rather arbitrary). As a validation of the method, Figure 3I displays the correlation between the apparent order parameter (expressed here as  $1 - S^2$ ) of the  $^1\text{H}$  NERRD fits (Figure 3F) with the exchange amplitude ( $\phi_{\text{ex}}$ )

derived from the high-temperature  $^{15}\text{N}$  BMRD fits (Figure 3E). The high correlation ( $R^2 = 0.83$ ) implies that these different experiments are indeed sensitive to the same type of motion, which, unlike  $^{15}\text{N}$  NERRD, does not necessarily have to involve motion of the reporting amide itself but can sense the motion in the surrounding. This motion sensed by  $^1\text{H}$  NERRD and  $^{15}\text{N}$  BMRD can infer changes in the homonuclear dipolar coupling network (apparent in  $^1\text{H}$  NERRD) or in the isotropic component of the  $^{15}\text{N}$  chemical shielding tensor (apparent in  $^{15}\text{N}$  BMRD). The fact that these two measures correlate suggests that the isotropic chemical-shift fluctuations detected in  $^{15}\text{N}$  BMRD are due to structural changes, including movements of protons (rather than solely reflecting side-chain jumps), which result in changes in charge distributions or ring-current contribution to chemical shifts.

Figure 3A summarizes the findings of the  $^1\text{H}$  and  $^{15}\text{N}$  solution- and solid-state dispersion studies. In general, all of these techniques identify similar sites that are involved in microsecond time-scale motion. Most of these sites are located at the RT and N-Src loop: S19, R21, and T24 show relaxation dispersion in all of the five dispersion experiments, while L8, E22, T37, and N38 have dispersion in four measurement types. The consistency among the residues for which we detect microsecond time-scale motion in these measurements confirms the validity of all of these solid-state dispersion techniques for qualitative investigations of microsecond protein dynamics. Furthermore, the observed residue-specific differences between  $^1\text{H}$  and  $^{15}\text{N}$  and between BMRD and NERRD techniques provides complementary insights into the details of the structural rearrangements.  $^1\text{H}$  relaxation grasps translational motion of the reporter relative to the environment,  $^{15}\text{N}$  BMRD detects changes in the chemical environment on a few hundreds of  $\mu\text{s}$  time scale, and  $^{15}\text{N}$  NERRD senses anisotropic, angular fluctuations of the  $^1\text{H}$ – $^{15}\text{N}$  bond itself on a tens of  $\mu\text{s}$  time scale. All of these pieces of information can be used to build putative models for the excited-state structures.

**Structure Interpretation.** To explore the structural basis of the conformational changes during the exchange processes, we performed an extensive structural bioinformatics survey of the Protein Data Bank (PDB) to identify potential alternative states of the protein. We used the room-temperature PDB structure 2NUZ to represent the ground state of  $\alpha$ -spectrin SH3 because the crystallization and data acquisition conditions ( $T = 20^\circ\text{C}$ ) were identical to those in this study. We gathered a data set of 335 SH3 domain crystal structures and searched for variants with distinct structural features.

In line with the high-temperature  $^1\text{H}$  NERRD and  $^{15}\text{N}$  BMRD relaxation data, the most recognizable difference in these structures is the peptide bond conformation at the tip of the RT loop (corresponding to P20–R21 in  $\alpha$ -spectrin SH3). The torsion angles at this site can be in either a standard right-handed  $\alpha$ -helix conformation ( $\alpha_{\text{R}}$ )  $\phi_{21} \approx -90^\circ$ , as observed in 2NUZ, or in a flipped, left-handed  $\alpha$ -helix conformation ( $\alpha_{\text{L}}$ ) with  $\phi_{21} \approx 90^\circ$ . In Ramachandran plots of the ensemble, a subset of all structures shows the  $\alpha_{\text{L}}$ , and most others show the  $\alpha_{\text{R}}$  conformation (Figure 5A). This is in agreement with a 10-fold greater preference of arginine for the  $\alpha_{\text{R}}$  conformation and also suggests that the  $\alpha_{\text{L}}$  conformation would be a low-populated excited state. Therefore, we suggest that the observed slow microsecond motion, present in amide angles at R21 as well as in amide shifts and proton dipolar couplings also around R21, is a consequence of the  $\sim 180^\circ$  flip of the

P20–R21 peptide plane. This putative collective and large-amplitude motion at the backbone of the RT loop represents a so far undescribed conformational switch at the SH3 binding interface, which occurs even in the absence of any bound ligand. The mode of the observed transition is reminiscent of the conformational preselection mechanism that has been observed for several catalytic, regulatory, or transport proteins.<sup>59–61</sup> A similar peptide flip has been also observed in ubiquitin crystals and in solution, where the flip of one bond initiates a collective global motion that regulates protein–protein interaction.<sup>15,62</sup>

To determine whether these two conformations are compatible with experimental data, we developed a method that predicts  $^1\text{H}$   $R_{1\rho}$  NERRD profiles from a set of crystal structure-derived conformations. The algorithm takes into account changes in distance and orientation between pairs of protons in the ensemble. For the purpose of SH3 analysis, we generated a set of two-member ensembles, with the ground-state member always 2NUZ. The other member, representing the hypothetical excited state, was taken from a subset of 99 structures that aligned to 2NUZ without any gaps (Figure S8). These pairs of structures represented the structural bases for the reconstruction of the  $^1\text{H}$  NERRD profiles as a sensitive, long-range reporter on relative structural changes. On the basis of the homonuclear  $^1\text{H}$ – $^1\text{H}$  interactions, we numerically calculated the autocorrelation function, assuming an exchange time scale of 60  $\mu\text{s}$  (the time scale was based on the fitted time-scale parameters of the  $^1\text{H}$  NERRD profiles, see Figure 4 bottom panel), which was then Fourier transformed to yield the spectral density function. By substituting the obtained  $J(\omega)$  values into the analytical equation (eq 2), we obtained simulated  $^1\text{H}$  NERRD profiles, which we then compared with the experimental relaxation data (see SI for further details on the procedure). This comparison was pursued in a 2-fold fashion using both correlation coefficients as well as root-mean-square deviations (RMSD) (Figure 5B). Both metrics show that putative excited states having an  $\alpha_{\text{L}}$  peptide conformation predict trends in the  $^1\text{H}$  NERRD data significantly better than an  $\alpha_{\text{R}}$  peptide conformation, consistent with the hypothesis that the peptide bond rotation is involved in microsecond motion. The best ensemble shows remarkable agreement between the simulated and the experimental data, with the largest displacement around the R21 amide proton (3.2 Å, Figure 5C), matching the  $^{15}\text{N}$  NERRD data as a local reporter of the process (Figure 3D). Furthermore, the ensemble captures not only the relative magnitudes between different residues found experimentally but also the lack of measurable  $^1\text{H}$  NERRD at residues like V23 (Figure 5D and S9). Even though the quantification of  $^1\text{H}$  relaxation for dynamics is still affected by unsuppressed coherent effects and by homonuclear recoupling, the correlation between the amplitudes of  $^{15}\text{N}$  BMRD and  $^1\text{H}$  NERRD (Figure 3I) suggests that slow-motional characteristics are properly reflected by  $^1\text{H}$  relaxation data on a qualitative or semi-quantitative level.

Grasping the structural changes during the faster microsecond time-scale motion is more challenging because only a few sites (e.g., E7, L8, R21, W41N $\epsilon$ 1, R49, and D62 at  $20^\circ\text{C}$ ) show notable motions in the  $^{15}\text{N}$  NERRD data sets (Figure 3D), most of which are in loops or at the termini. At  $0^\circ\text{C}$ , these sites include E7, L8, R21, V23, K39, W41N $\epsilon$ 1, V46, R49, Q50, and D62 (Figure 3B,G). In the solid state, the HN cross-peaks of N47 and D48 are absent both in the CP-based and in



the INEPT-based  $^1\text{H}$ – $^{15}\text{N}$  correlation spectra for any of the conditions we employed, indicating that high-amplitude microsecond–millisecond time-scale conformational exchange broadens those peaks beyond detection. It is reasonable to expect that the neighboring residues, V46, R49, and Q50, are affected by the same loop motion. Similarly, R21 and K39, at the tip of the RT and N-Src loops, and E7, L8, and D62 at the N- and C-termini, have higher flexibility than the rigid  $\beta$ -sheets. The relatively low-amplitude (Figure 3B) fast microsecond motion detected for most other sites at 0 °C may stem from intrinsic amide bond fluctuations or low-amplitude “rocking motion”. Such rocking motion has been observed for SH3 and for other microcrystalline proteins,<sup>13,15,19,63</sup> and it seems to be a general phenomenon in crystalline samples. This overall motion becomes elusive when the temperature is increased to 20 °C or above. In the  $^{15}\text{N}$  NERRD recorded at 20 °C, we see two motionally distinct groups (cf. Figure 4 upper panel), namely a group of faster moving sites with  $\tau_{\text{ex}} \approx 5 \mu\text{s}$  (E7, R21, W41N $\epsilon$ 1, and D62) and a group of more slowly moving sites with  $\tau_{\text{ex}} \approx 60 \mu\text{s}$  (N35N $\delta$ , S36, T37, N38, R49, and Q50N $\epsilon$ ). These latter residues report on the mobility of the N-Src and distal loops on a wide range of time scales. The collective, fast microsecond motion of the seemingly distant E7, R21, W41N $\epsilon$ 1, and D62 nitrogens deserves a closer look at X-ray structures to elucidate the possible underlying mechanism. By inspecting the ground-state structure of SH3 (PDB: 2NUZ), one can recognize that the guanidium group of the R21 side chain forms a cation– $\pi$  complex with the indole ring of W41. In the crystal structure, these residues are in crystal–crystal contact with E7 and L61 of the neighboring molecule (Figure S10). Presumably, D62 is also involved in the crystal contact; however, it lacks resolvable density in the X-ray structure, and thus its exact position is ambiguous. We speculate that the side-chain rotation of R21 initiates the observed  $\sim 5 \mu\text{s}$  motion as it moves from a closed to an open conformation, represented by the crystal structure 1U06. For the R21 side chain to move away, for steric reasons in the crystal, a reorganization of the N- and C-termini needs to take place, the likely reason for the slow-down of the side-chain rotation to the microsecond regime. However, determination of the exact mechanism behind the faster motion is complicated by the lack of coordinates for the first six N-terminal residues (MDETGK) and the last C-terminal residue (D) for both 2NUZ and 1U06 crystal structures.  $^{15}\text{N}$  NERRD measurements of an R21A mutant might further clarify the mechanistic details of the observed microsecond time-scale motion. However, such measurements were outside the scope of the current study.

In the solution state, R21 is solvent exposed and no crystal–crystal contact hinders its side-chain rotations. Such a motion should happen on a much faster time scale ( $\tau_{\text{ex}} \ll 1 \mu\text{s}$ ), outside the Bloch–McConnell dispersion regime. Instead, the observed fast microsecond motion in solution-state  $^1\text{H}$  BMRD around the RT loop residues presumably represents the described R21 peptide plane flip. Due to the absence of crystal crowding, this conformational exchange is accelerated several-fold with respect to the rate in solid crystals. Similar differences in microsecond time-scale motion (solids vs solution) have been observed for ubiquitin.<sup>15</sup>

It is possible that the observed conformational rearrangements play a role in regulating the ligand binding and specificity of  $\alpha$ -spectrin SH3 (Figure 6A). Although so far no high-affinity  $\alpha$ -spectrin SH3 ligands have been described, and

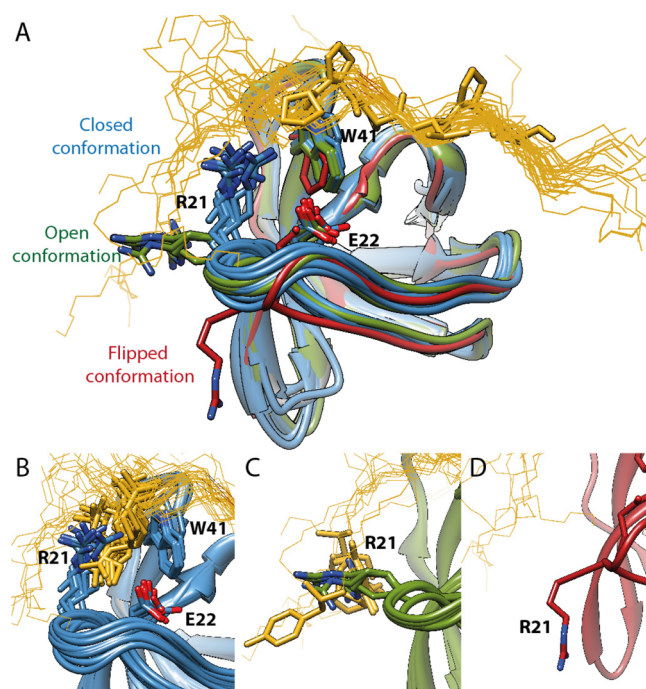


**Figure 6.** R21 may regulate the ligand-binding of SH3. (A) Ribbon representation of 18  $\alpha$ -spectrin SH3 structures displayed together with ligands (gold wires) from other SH3 complexes; the only  $\alpha$ -spectrin-bound ligand is displayed with sticks (3THK). (B–D) Three alternative R21 orientations in close-up views. Ligand backbones and clashing side chains are displayed with wires and sticks. (B) In the closed conformation R21 sterically blocks many SH3 ligands as it clashes with the peptide side chains that enter the specificity pocket. (C) The open conformation allows the ligand to enter the specificity pocket (E22) but prevents the binding of longer peptides. (D) In the flipped conformation (1H8K) no protein–ligand clash is expected.

the only ligand-bound crystal structure stems from a chimeric fusion protein (PDB: 3THK<sup>64</sup>), the comparison to other SH3–ligand complexes (Figure 6) suggests the flipping motion might have functional relevance. In the ground-state apo form, by forming a salt-bridge with E22 in the specificity pocket and a cation– $\pi$  interaction with W41 at the Px-binding pocket (Figure 6B), R21 would block any ligand binding. To accommodate binding partners, especially those with positively charged residues that enter the specificity pocket, R21 must at a minimum move to an open conformation, where the side chain is bent away but the backbone has not yet flipped and the cation– $\pi$  interaction is broken (Figure 6C). However, only the P20–R21 peptide-bond-flipped conformation would allow the binding of even longer peptides (Figure 6D). Binding studies of R21-mutated  $\alpha$ -spectrin SH3 corroborate this idea,<sup>65</sup> the R21A mutant shows 3 to 4 times higher affinity toward the decapeptide p41 than the wild-type SH3 does. Other unidentified allosteric binding partners might further increase the equilibrium population of the R21 excited state, thereby influencing the ligand binding probability.

## CONCLUSIONS

In this study, we have demonstrated that the joint analysis of solid-state  $^1\text{H}$  and  $^{15}\text{N}$  relaxation dispersion measurements gives a complementary view on microsecond time-scale protein dynamics. The rotating-frame relaxation of  $^{15}\text{N}$  conveys the environmental changes in BMRD experiments, while it detects local angular reorientations in NERRD measurements.  $^1\text{H}$   $R_{1\rho}$

relaxation, on the other hand, is always influenced by the motion of the protonated neighborhood through the strong  $^1\text{H}$ – $^1\text{H}$  dipolar coupling (in particular in NERRD experiments with  $B_1$  fields near the HORROR condition), and thus it is rather a sensor of global rearrangements than of local fluctuations. The combination of the complementary  $^{15}\text{N}$  and  $^1\text{H}$  relaxation dispersion techniques, measured at low rf field strengths and near the rotary-resonance conditions, facilitates the mechanistic description of protein motion. To obtain accurate motional parameters, it is inevitable to sample the  $R_{1\rho}$  relaxation rates at multiple spin-lock field strengths and/or spinning frequencies; otherwise, the model fitting would be biased toward time-scale regimes where transverse relaxation rates are the most sensitive.<sup>20,46</sup>

Using this comprehensive solid-state relaxation-dispersion-based approach, we identified a two-step collective microsecond motion at the ligand recognition loop of the  $\alpha$ -spectrin SH3 domain. The various RD data are in remarkable agreement with a structural model in which, first, the R21 side chain rotates into an open conformation where the R21...W41 cation– $\pi$  interaction breaks and, in the next step, the detachment enables a  $\sim 180^\circ$  flip at the P20–R21 peptide bond. Steric implications of the transition at the binding interface, occurring in the absence of bound ligand, suggest a conformational-preselection mechanism for this SH3 domain. From a methodological point of view, we have demonstrated that  $^1\text{H}$  NERRD experiments can assist  $^{15}\text{N}$  relaxation dispersion techniques as sensitive, qualitative reporters for large-scale structural rearrangements involving translational motions and side-chain reorientations. Furthermore, we have introduced a structural bioinformatics method which enables the selection of the likely excited-state conformations from a large set of crystal structures based on the comparison of experimental and simulated dispersion profiles. The combination of the different dispersion techniques, reporter nuclei, and computational methods is essential to gain structural insights into the source of the observed dispersion effects. Despite the remaining open questions regarding the quantification of  $^1\text{H}$  solid-state relaxation data, our study demonstrates the potential of solid-state NMR on perdeuterated samples for sensitive detection of protein functional dynamics occurring on the microsecond time scale.

## ■ ASSOCIATED CONTENT

### ■ Supporting Information

The Supporting Information is available free of charge on the ACS Publications website at DOI: 10.1021/jacs.8b09258.

Detailed methods, pulse sequences for relaxation measurements, details of the fitting procedures, quantification of errors and inaccuracies, experimental relaxation dispersion profiles, and SH3 sequence alignment (PDF)

## ■ AUTHOR INFORMATION

### Corresponding Author

\*rasmus.linser@lmu.de

### ORCID

Petra Rovó: 0000-0001-8729-7326

Bert L. de Groot: 0000-0003-3570-3534

Paul Schanda: 0000-0002-9350-7606

Rasmus Linser: 0000-0001-8983-2935

## Notes

The authors declare no competing financial interest.

## ■ ACKNOWLEDGMENTS

We thank Karin Giller and Stefan Becker for the protein preparation, Matthias Ernst and Christian Griesinger for helpful discussions, and Supriya Pratihari for assistance in solution-state NMR measurements and data analysis. We thank Anne Diehl and Kristina Rehbein (FMP Berlin) for their kind support with respect to protein purification. The authors acknowledge support from the Deutsche Forschungsgemeinschaft (SFB 749, project A11, SFB 1309, project A3, and the Emmy Noether program), the European Research Council (ERC-Stg-2012-311318-Prot-Dyn2Function), Center for NanoScience, the Excellence Clusters CIPSM and RESOLV, the Max Planck Society, and Fonds der Chemischen Industrie.

## ■ REFERENCES

- (1) Giraud, N.; Blackledge, M.; Goldman, M.; Böckmann, A.; Lesage, A.; Penin, F.; Emsley, L. Quantitative analysis of backbone dynamics in a crystalline protein from nitrogen-15 spin-lattice relaxation. *J. Am. Chem. Soc.* **2005**, *127*, 18190–18201.
- (2) Krushelnitsky, A.; Reichert, D.; Saalwächter, K. Solid-state NMR approaches to internal dynamics of proteins: from picoseconds to microseconds and seconds. *Acc. Chem. Res.* **2013**, *46*, 2028–2036.
- (3) Lewandowski, J. R. Advances in solid-state relaxation methodology for probing site-specific protein dynamics. *Acc. Chem. Res.* **2013**, *46*, 2018–2027.
- (4) Schanda, P.; Ernst, M. Studying Dynamics by Magic-Angle Spinning Solid-State NMR Spectroscopy: Principles and Applications to Biomolecules. *Prog. Nucl. Magn. Reson. Spectrosc.* **2016**, *96*, 1–46.
- (5) Schubeis, T.; Le Marchand, T.; Andreas, L. B.; Pintacuda, G.  $^1\text{H}$  magic-angle spinning NMR evolves as a powerful new tool for membrane proteins. *J. Magn. Reson.* **2018**, *287*, 140–152.
- (6) Loquet, A.; El Mhammeri, N.; Stanek, J.; Berbon, M.; Bardiaux, B.; Pintacuda, G.; Habenstein, B. 3D structure determination of amyloid fibrils using solid-state NMR spectroscopy. *Methods* **2018**, *138–139*, 26–38.
- (7) Quinn, C. M.; Lu, M.; Suiter, C. L.; Hou, G.; Zhang, H.; Polenova, T. Magic angle spinning NMR of viruses. *Prog. Nucl. Magn. Reson. Spectrosc.* **2015**, *86–87*, 21–40.
- (8) Tollinger, M.; Sivertsen, A. C.; Meier, B. H.; Ernst, M.; Schanda, P. Site-resolved measurement of microsecond-to-millisecond conformational-exchange processes in proteins by solid-state NMR spectroscopy. *J. Am. Chem. Soc.* **2012**, *134*, 14800–14807.
- (9) Ma, P.; Haller, J. D.; Zajackala, J.; Macek, P.; Sivertsen, A. C.; Willbold, D.; Boisbouvier, J.; Schanda, P. Probing transient conformational states of proteins by solid-state  $R_{1\rho}$  relaxation-dispersion NMR spectroscopy. *Angew. Chem., Int. Ed.* **2014**, *53*, 4312–4317.
- (10) Quinn, C. M.; McDermott, A. E. Monitoring conformational dynamics with solid-state  $R_{1\rho}$  experiments. *J. Biomol. NMR* **2009**, *45*, 5–8.
- (11) Quinn, C. M.; McDermott, A. E. Quantifying conformational dynamics using solid-state  $R_{1\rho}$  experiments. *J. Magn. Reson.* **2012**, *222*, 1–7.
- (12) Lamley, J. M.; Öster, C.; Stevens, R. A.; Lewandowski, J. R. Intermolecular Interactions and Protein Dynamics by Solid-State NMR Spectroscopy. *Angew. Chem., Int. Ed.* **2015**, *54*, 15374–15378.
- (13) Smith, A. A.; Testori, E.; Cadalbert, R.; Meier, B. H.; Ernst, M. Characterization of fibril dynamics on three timescales by solid-state NMR. *J. Biomol. NMR* **2016**, *65*, 171–191.
- (14) Gauto, D. F.; Hessel, A.; Rovó, P.; Kurauskas, V.; Linser, R.; Schanda, P. Protein conformational dynamics studied by  $^{15}\text{N}$  and  $^1\text{H}$   $R_{1\rho}$  relaxation dispersion: Application to wild-type and G53A ubiquitin crystals. *Solid State Nucl. Magn. Reson.* **2017**, *87*, 86–95.
- (15) Kurauskas, V.; Izmailov, S. A.; Rogacheva, O. N.; Hessel, A.; Ayala, I.; Woodhouse, J.; Shilova, A.; Xue, Y.; Yuwen, T.; Coquelle,



N.; et al. Slow conformational exchange and overall rocking motion in ubiquitin protein crystals. *Nat. Commun.* **2017**, *8*, 145.

(16) Rovó, P.; Linser, R. Microsecond Time Scale Proton Rotating-Frame Relaxation under Magic Angle Spinning. *J. Phys. Chem. B* **2017**, *121*, 6117–6130.

(17) Smith, A. A.; Ernst, M.; Meier, B. H. Because the Light is Better Here: Correlation-Time Analysis by NMR Spectroscopy. *Angew. Chem., Int. Ed.* **2017**, *56*, 13590–13595.

(18) Lakomek, N.-A.; Penzel, S.; Lends, A.; Cadalbert, R.; Ernst, M.; Meier, B. H. Microsecond Dynamics in Ubiquitin Probed by Solid-State  $^{15}\text{N}$  NMR Spectroscopy  $R_{1\rho}$  Relaxation Experiments under Fast MAS (60–110kHz). *Chem. - Eur. J.* **2017**, *23*, 9425–9433.

(19) Krushelnitsky, A.; Gauto, D.; Rodriguez Camargo, D. C.; Schanda, P.; Saalwächter, K. Microsecond motions probed by near-rotary-resonance  $R_{1\rho}$   $^{15}\text{N}$  MAS NMR experiments: the model case of protein overall-rocking in crystals. *J. Biomol. NMR* **2018**, *71*, 53–67.

(20) Smith, A. A.; Ernst, M.; Meier, B. H. Optimized “detectors” for dynamics analysis in solid-state NMR. *J. Chem. Phys.* **2018**, *148*, No. 045104.

(21) Rovó, P.; Linser, R. Microsecond Timescale Protein Dynamics: a Combined Solid-State NMR Approach. *ChemPhysChem* **2018**, *19*, 34–39.

(22) Shannon, M.; Theint, T.; Mukhopadhyay, D.; Surewicz, K.; Surewicz, W.; Marion, D.; Schanda, P.; Jaroniec, C. P. Conformational Dynamics in the Core of Human Y145Stop Prion Protein Amyloid Probed by Relaxation Dispersion NMR. *ChemPhysChem* **2018**, DOI: 10.1002/cphc.201800779

(23) Keeler, E. G.; Fritzsche, K. J.; McDermott, A. E. Refocusing CSA during magic angle spinning rotating-frame relaxation experiments. *J. Magn. Reson.* **2018**, *296*, 130–137.

(24) Lewandowski, J. R.; Sass, H. J.; Grzesiek, S.; Blackledge, M.; Emsley, L. Site-specific measurement of slow motions in proteins. *J. Am. Chem. Soc.* **2011**, *133*, 16762–16765.

(25) Zinkevich, T.; Chevelkov, V.; Reif, B.; Saalwächter, K.; Krushelnitsky, A. Internal protein dynamics on ps to us timescales as studied by multi-frequency  $^{15}\text{N}$  solid-state NMR relaxation. *J. Biomol. NMR* **2013**, *57*, 219–235.

(26) Lewandowski, J. R.; Sein, J.; Blackledge, M.; Emsley, L. Anisotropic collective motion contributes to nuclear spin relaxation in crystalline proteins. *J. Am. Chem. Soc.* **2010**, *132*, 1246–1248.

(27) Yu, H.; Rosen, M. K.; Shin, T. B.; Seidel-Dugan, C.; Brugge, J. S.; Schreiber, S. L. Solution structure of the SH3 domain of Src and identification of its ligand-binding site. *Science* **1992**, *258*, 1665–1668.

(28) Ball, L. J.; Kühne, R.; Schneider-Mergener, J.; Oschkinat, H. Recognition of proline-rich motifs by protein-protein-interaction domains. *Angew. Chem., Int. Ed.* **2005**, *44*, 2852–2869.

(29) Stahl, M. L.; Ferez, C. R.; Kelleher, K. L.; Kriz, R. W.; Knopf, J. L. Sequence similarity of phospholipase C with the non-catalytic region of src. *Nature* **1988**, *332*, 269–272.

(30) Ren, R.; Mayer, B. J.; Cicchetti, P.; Baltimore, D. Identification of a ten-amino acid proline-rich SH3 binding site. *Science* **1993**, *259*, 1157–1161.

(31) Larson, S. M.; Davidson, A. R. The identification of conserved interactions within the SH3 domain by alignment of sequences and structures. *Protein Sci.* **2000**, *9*, 2170–2180.

(32) Kaneko, T.; Sidhu, S. S.; Li, S. S. C. Evolving specificity from variability for protein interaction domains. *Trends Biochem. Sci.* **2011**, *36*, 183–190.

(33) Chevelkov, V.; Rehbein, K.; Diehl, A.; Reif, B. Ultrahigh resolution in proton solid-state NMR spectroscopy at high levels of deuteration. *Angew. Chem., Int. Ed.* **2006**, *45*, 3878–3881.

(34) Linser, R.; Chevelkov, V.; Diehl, A.; Reif, B. Sensitivity enhancement using paramagnetic relaxation in MAS solid-state NMR of perdeuterated proteins. *J. Magn. Reson.* **2007**, *189*, 209–216.

(35) Chevelkov, V.; Zhuravleva, A. V.; Xue, Y.; Reif, B.; Skrynnikov, N. R. Combined analysis of  $^{15}\text{N}$  relaxation data from solid- and solution-state NMR spectroscopy. *J. Am. Chem. Soc.* **2007**, *129*, 12594–12595.

(36) Chevelkov, V.; Xue, Y.; Linser, R.; Skrynnikov, N. R.; Reif, B. Comparison of solid-state dipolar couplings and solution relaxation data provides insight into protein backbone dynamics. *J. Am. Chem. Soc.* **2010**, *132*, 5015–5017.

(37) Linser, R.; Fink, U.; Reif, B. Assignment of dynamic regions in biological solids enabled by spin-state selective NMR experiments. *J. Am. Chem. Soc.* **2010**, *132*, 8891–8893.

(38) Chevelkov, V.; Fink, U.; Reif, B. Quantitative analysis of backbone motion in proteins using MAS solid-state NMR spectroscopy. *J. Biomol. NMR* **2009**, *45*, 197–206.

(39) Redfield, A. G. On the Theory of Relaxation Processes. *IBM J. Res. Dev.* **1957**, *1*, 19–31.

(40) Palmer, A. G.; Massi, F. Characterization of the dynamics of biomacromolecules using rotating-frame spin relaxation NMR spectroscopy. *Chem. Rev.* **2006**, *106*, 1700–1719.

(41) VanderHart, D. L.; Garroway, A. N.  $^{13}\text{C}$  NMR rotating frame relaxation in a solid with strongly coupled protons: Polyethylene. *J. Chem. Phys.* **1979**, *71*, 2773.

(42) Akasaka, K.; Ganapathy, S.; McDowell, C. A.; Naito, A. Spin-spin and spin-lattice contributions to the rotating-frame relaxation of  $^{13}\text{C}$  in L-alanine. *J. Chem. Phys.* **1983**, *78*, 3567–3572.

(43) Kurbanov, R.; Zinkevich, T.; Krushelnitsky, A. The nuclear magnetic resonance relaxation data analysis in solids: general  $R_1/R_{1\rho}$  equations and the model-free approach. *J. Chem. Phys.* **2011**, *135*, 184104.

(44) Linser, R.; Fink, U.; Reif, B. Probing surface accessibility of proteins using paramagnetic relaxation in solid-state NMR spectroscopy. *J. Am. Chem. Soc.* **2009**, *131*, 13703–13708.

(45) Eichmüller, C.; Skrynnikov, N. R. A new amide proton  $R_{1\rho}$  experiment permits accurate characterization of microsecond timescale conformational exchange. *J. Biomol. NMR* **2005**, *32*, 281–293.

(46) Smith, C. A.; Ban, D.; Pratihari, S.; Giller, K.; Schwiagk, C.; de Groot, B. L.; Becker, S.; Griesinger, C.; Lee, D. Population shuffling of protein conformations. *Angew. Chem., Int. Ed.* **2015**, *54*, 207–210.

(47) Mulder, F. A. A.; de Graaf, R. A.; Kaptein, R.; Boelens, R. An Off-resonance Rotating Frame Relaxation Experiment for the Investigation of Macromolecular Dynamics Using Adiabatic Rotations. *J. Magn. Reson.* **1998**, *131*, 351–357.

(48) Shaka, A. J.; Keeler, J.; Frenkiel, T.; Freeman, R. An improved sequence for broadband decoupling: WALTZ-16. *J. Magn. Reson.* **1983**, *52*, 335–338.

(49) Zhou, D. H.; Rienstra, C. M. High-performance solvent suppression for proton detected solid-state NMR. *J. Magn. Reson.* **2008**, *192*, 167–172.

(50) Altschul, S. F.; Madden, T. L.; Schäffer, A. A.; Zhang, J.; Zhang, Z.; Miller, W.; Lipman, D. J. Gapped BLAST and PSI-BLAST: a new generation of protein database search programs. *Nucleic Acids Res.* **1997**, *25*, 3389–3402.

(51) Word, J. M.; Lovell, S. C.; Richardson, J. S.; Richardson, D. C. Asparagine and glutamine: using hydrogen atom contacts in the choice of side-chain amide orientation. *J. Mol. Biol.* **1999**, *285*, 1735–1747.

(52) Leaver-Fay, A.; Tyka, M.; Lewis, S. M.; Lange, O. F.; Thompson, J.; Jacak, R.; Kaufmann, K. W.; Renfrew, P. D.; Smith, C. A.; Sheffler, W.; et al. ROSETTA3: An Object Oriented Software Suite for the Simulation and Design of Macromolecules. *Methods Enzymol.* **2011**, *487*, 545–574.

(53) Peter, C.; Daura, X.; van Gunsteren, W. F. Calculation of NMR-relaxation parameters for flexible molecules from molecular dynamics simulations. *J. Biomol. NMR* **2001**, *20*, 297–310.

(54) Goddard, T.; Kneller, D. G. SPARKY 3; 1999.

(55) Lee, W.; Tonelli, M.; Markley, J. L. NMRFAM-SPARKY: enhanced software for biomolecular NMR spectroscopy. *Bioinformatics* **2015**, *31*, 1325–1327.

(56) Clore, G. M.; Szabo, A.; Bax, A.; Kay, L. E.; Driscoll, P. C.; Gronenborn, A. M. Deviations from the simple two-parameter model-free approach to the interpretation of nitrogen-15 nuclear magnetic relaxation of proteins. *J. Am. Chem. Soc.* **1990**, *112*, 4989–4991.



(57) Haller, J. D.; Schanda, P. Amplitudes and time scales of picosecond-to-microsecond motion in proteins studied by solid-state NMR: a critical evaluation of experimental approaches and application to crystalline ubiquitin. *J. Biomol. NMR* **2013**, *57*, 263–280.

(58) Nielsen, N. C.; Bildsoe, H.; Jakobsen, H. J.; Levitt, M. H. Double-quantum homonuclear rotary resonance: Efficient dipolar recovery in magic-angle spinning nuclear magnetic resonance. *J. Chem. Phys.* **1994**, *101*, 1805–1812.

(59) Eisenmesser, E. Z.; Millet, O.; Labeikovsky, W.; Korzhnev, D. M.; Wolf-Watz, M.; Bosco, D. A.; Skalicky, J. J.; Kay, L. E.; Kern, D. Intrinsic dynamics of an enzyme underlies catalysis. *Nature* **2005**, *438*, 117–121.

(60) Tang, C.; Schwieters, C. D.; Clore, G. M. Open-to-closed transition in apo maltose-binding protein observed by paramagnetic NMR. *Nature* **2007**, *449*, 1078–1082.

(61) van den Bedem, H.; Fraser, J. S. Integrative, dynamic structural biology at atomic resolution—it's about time. *Nat. Methods* **2015**, *12*, 307–318.

(62) Smith, C. A.; Ban, D.; Pratihar, S.; Giller, K.; Paulat, M.; Becker, S.; Griesinger, C.; Lee, D.; de Groot, B. L. Allosteric switch regulates protein-protein binding through collective motion. *Proc. Natl. Acad. Sci. U. S. A.* **2016**, *113*, 3269–3274.

(63) Ma, P.; Xue, Y.; Coquelle, N.; Haller, J. D.; Yuwen, T.; Ayala, I.; Mikhailovskii, O.; Willbold, D.; Colletier, J.-P.; Skrynnikov, N. R.; et al. Observing the overall rocking motion of a protein in a crystal. *Nat. Commun.* **2015**, *6*, 8361.

(64) Gushchina, L. V.; Gabdulkhakov, A. G.; Nikonov, S. V.; Filimonov, V. V. High-resolution crystal structure of spectrin SH3 domain fused with a proline-rich peptide. *J. Biomol. Struct. Dyn.* **2011**, *29*, 485–495.

(65) Casares, S.; Ab, E.; Eshuis, H.; Lopez-Mayorga, O.; van Nuland, N. A. J.; Conejero-Lara, F. The high-resolution NMR structure of the R21A Spc-SH3:P41 complex: understanding the determinants of binding affinity by comparison with Abl-SH3. *BMC Struct. Biol.* **2007**, *7*, 22.